

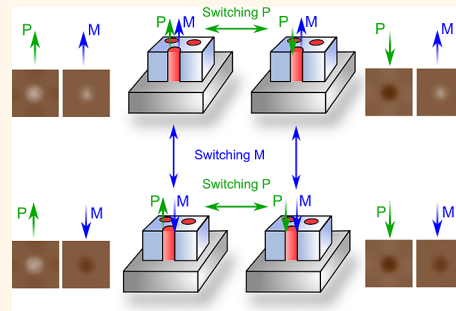
Four-States Multiferroic Memory Embodied Using Mn-Doped BaTiO₃ Nanorods

Jong Yeog Son,[†] Jung-Hoon Lee,[‡] Seungwoo Song,[‡] Young-Han Shin,[§] and Hyun Myung Jang^{‡,*}

[†]Department of Applied Physics, College of Applied Science, Kyung Hee University, Suwon 446-701, Republic of Korea, [‡]Department of Materials Science and Engineering, and Division of Advanced Materials Science, Pohang University of Science and Technology (POSTECH), Pohang 790-784, Republic of Korea, and

[§]Department of Physics and EHSRC, University of Ulsan, Ulsan 680-749, Republic of Korea

ABSTRACT Multiferroics that show simultaneous ferroic responses have received a great deal of attention by virtue of their potential for enabling new device paradigms. Here, we demonstrate a high-density four-states multiferroic memory using vertically aligned Mn-doped BaTiO₃ nanorods prepared by applying the dip-pen nanolithography technique. In the present nanorods array, the polarization (P) switching by an external electric field does not influence the magnetization (M) of the nanorod owing to a negligible degree of the P–M cross-coupling. Similarly, the magnetic-field-induced M switching is unaffected by the ferroelectric polarization. On the basis of these, we are able to implement a four-states nonvolatile multiferroic memory, namely, (+P,+M), (+P,-M), (-P,+M), and (-P,-M) with the reliability in the P and M switching. Thus, the present work makes an important step toward the practical realization of multistate ferroic memories.



KEYWORDS: four-states memory · multiferroic memory · polarization-magnetization cross-coupling · Mn-doped BaTiO₃ nanorods · piezoelectric force microscopy · magnetic force microscopy

Multiferroic materials exhibit simultaneous ferroic properties such as ferroelectricity, ferromagnetism, and ferroelasticity with coupled electric, magnetic, and structural order parameters.^{1–10} Multiferroics have received a great deal of attention by virtue of their fascinating physics of order-parameter cross-couplings^{2–4} and their potential for enabling new device paradigms^{4–8} which typically exploit a strong cross-coupling between polarization (**P**) and magnetization (**M**) vectors, as exemplified by a magnetic-field-control of the polarization flipping or switching^{2,3} and, *vice versa*, an electric-field-control of the magnetization or magnetic phase^{4,11,12} at cryogenic temperatures. Thus, a strong **P**–**M** cross-coupling at room temperature has been considered to be necessary for device applications of multiferroism.

Currently, BiFeO₃-based perovskites^{1,13,14} are the most well-known examples of room-temperature multiferroics. Single crystals of BiFeO₃ (BFO) having orthorhombic *R*3c

symmetry showed a noticeable degree of the **P**–**M** cross-coupling by exhibiting a spin flopping¹² or a change in the magnetic state¹⁵ in response to the polarization reorientation which is induced by an external electric field. Lebeugle *et al.*¹² showed that the polarization-reorientation-induced spin flopping is closely related to the cycloidal spin state which is characteristic of the stress-free bulk BFO having *R*3c symmetry. Thus, it is highly unlikely to expect a strong **P**–**M** cross-coupling in constrained thin films or nanorods of BFO where the spin cycloid is absent.^{12,16} More recently, single-crystal slices of PZTFT (lead zirconium titanate-lead iron tantalate) having complex ferroelectric domain structures also showed a strong room-temperature magnetoelectric (ME) coupling by demonstrating changes in the ferroelectric domain patterns under a bias magnetic field.¹⁷ However, this strong coupling has not been shown in a PZTFT nanorod having a single domain. Thus, practical implementation of multiferroic devices that requires a strong room-temperature

* Address correspondence to hmjang@postech.ac.kr.

Received for review April 9, 2013 and accepted May 29, 2013.

Published online May 29, 2013
10.1021/nn4017422

© 2013 American Chemical Society

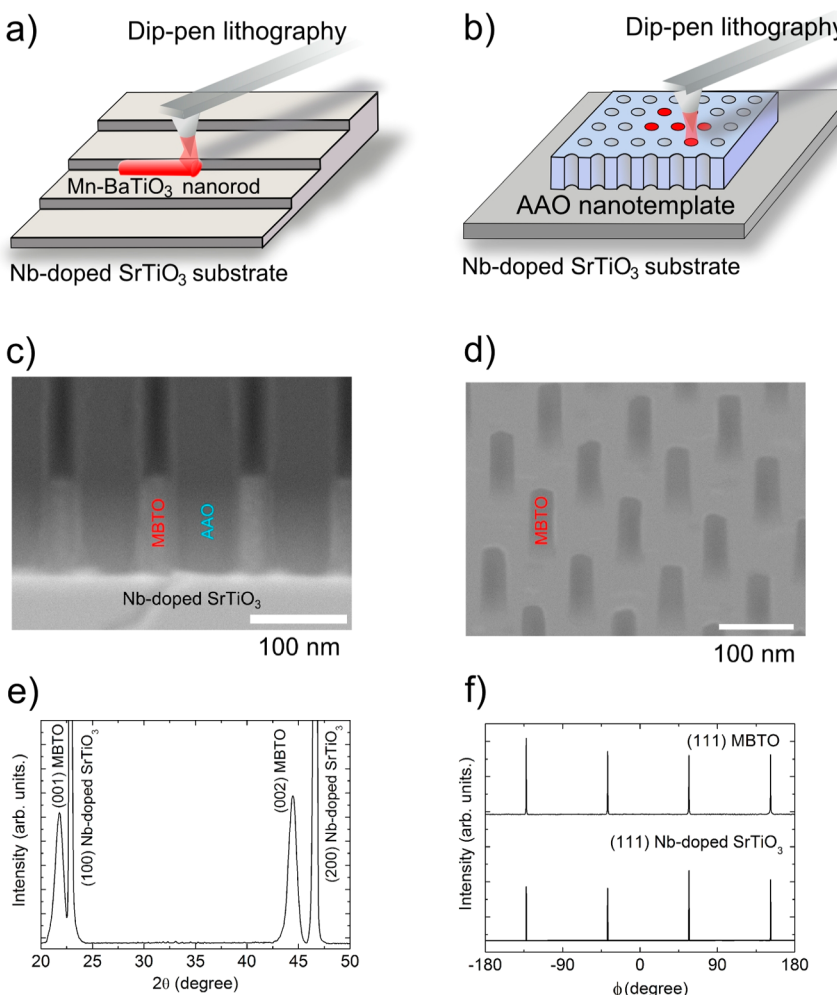


Figure 1. Fabrication of Mn-doped BaTiO_3 (M-BTO) nanorods array by dip-pen nanolithography (DPN), and structural characterizations of the vertically aligned 2 atom % Mn-doped BTO nanorods array. (a) Fabrication of laterally aligned M-BTO nanorods along terrace edges of the Nb-doped STO substrate using DPN. (b) Fabrication of vertically aligned M-BTO nanorods by filling the precursor solution into nanopores of the AAO nanotemplate using DPN. (c) A cross-sectional SEM image of the vertically aligned M-BTO nanorods array before the removal of the AAO nanotemplate. (d) A SEM image of the vertically aligned M-BTO nanorods array after the removal of the nanotemplate. (e) Theta-2theta X-ray diffraction pattern of the vertically aligned nanorods array grown on the (100) surface of the Nb-STO substrate. (f) Phi-scan spectra of the vertically aligned M-BTO nanorods array and the Nb-doped STO substrate.

P–M cross-coupling is still difficult to achieve and seems to be a challenging task. This is especially true for high-density devices that prefer nanorods to bulk single crystals.

In view of the difficulty associated with practical implementation of high-density multiferroic devices that require a strong room-temperature ME coupling, it is of great scientific and technological interest to propose an alternative multiferroic device that does not require any **P–M** cross-coupling. In this case, the **P** switching by an applied electric field does not affect the magnetization owing to a negligible degree of the **P–M** cross-coupling. Similarly, the polarization is not affected by the **M** switching caused by a bias magnetic field. Under these conditions, a four-states multiferroic memory is conceivable, *i.e.*, $(+P,+M)$, $(+P,-M)$, $(-P,+M)$, and $(-P,-M)$. To practically implement this type of ferroic memory, we have chosen a Mn-doped BaTiO_3

(abbreviated as M-BTO)^{18–20} as a promising candidate material since this system in a thin-film form is known to exhibit room-temperature multiferroism²⁰ with a negligible degree of the **P–M** cross-coupling. To achieve a high-density memory state, we have fabricated M-BTO nanorods either vertically or horizontally aligned on a Nb-doped SrTiO_3 (Nb-STO) substrate.

RESULTS AND DISCUSSION

Figure 1 schematically depicts the formation of laterally and vertically aligned M-BTO nanorods on a Nb-STO bottom-electrode substrate by utilizing the dip-pen nanolithography (DPN) method^{21,22} with a precursor sol for 2 atom % Mn-doped BaTiO_3 . For the fabrication of laterally aligned nanorods, we suitably combined the DPN method with a ‘step-edge decoration’ technique (Figure 1a). This step-edge decoration technique^{23,24} is efficient to form a nanorod along the

terrace edge as the edges are energetically favorable for the crystallization of adatoms. On the other hand, vertically aligned M-BTO nanorods were fabricated using an anodizing aluminum oxide (AAO) nanotemplate on a Nb-STO substrate (Figure 1b). The 100-nm-thick AAO nanotemplate with a pore diameter of 30 nm and an interpore distance of 100 nm was prepared by anodizing a 1.6- μ m-thick Al film. We then filled the M-BTO precursor sol in nanopores of the AAO nanotemplate to form vertically aligned nanorods (Figure 1b). Detailed procedures of the preparation of the AAO nanotemplate are described in Figure S1 of Supporting Information.

Figure 1c shows a cross-sectional scanning electron microscopy (SEM) image of the vertically aligned M-BTO nanorods array before the removal of the AAO nanotemplate. The vertically aligned nanorods grown on a Nb-STO substrate are clearly visible after the removal of the nanotemplate (Figure 1d). It is estimated that the diameter and the length of the M-BTO nanorod are about 27 and 80 nm, respectively. The theta-2theta X-ray diffraction ($\theta - 2\theta$ XRD) pattern presented in Figure 1e indicates that the vertically aligned nanorods grown on a Nb-STO substrate are highly [001]-oriented with the absence of any minority peak. The growth direction of the nanorods array is confirmed by carrying out in-plane XRD phi-scan measurement. The phi-scan spectra were obtained by keeping the Bragg angle at (111) for both the nanorods and the substrate. As shown in Figure 1f, the four peaks that are 90° apart each other occur at the same azimuthal phi-angles for both the M-BTO nanorods array and the Nb-STO substrate, demonstrating a 4-fold tetragonal symmetry of the M-BTO nanorod. This, in turn, indicates that the direction of the ferroelectric polarization (\mathbf{P}) is either parallel or antiparallel to the axis direction of the vertically aligned nanorod.

A typical piezoelectric hysteresis loop of the vertically aligned nanorod (Figure 2a) shows an effective remanent piezoelectric constant (d_{33}) of ~ 75 pm/V which is substantially higher than that of the laterally aligned M-BTO nanorod. Figure 2b demonstrates a

weak ferromagnetic response of the vertically aligned M-BTO nanorods array at room temperature. *Ab initio* density-functional theory (DFT) calculations^{25,26} were performed to understand the Mn-doping effect. For this purpose, we adopted a $3a \times 3b \times 3c$ supercell that contains two Mn ions distributed among 27 BaTiO₃ formula cells (Figure 3a,b). Thus, the atomic fraction of the substituted Mn ions is $x = 2/27 \approx 7.4$ atom %. The computed off-center ferroelectric displacement of the substituted Mn ion in the MnO₆ octahedron unit is smaller than that of the unsubstituted Ti ion in the TiO₆ octahedron unit by 0.05 Å, with a concomitant decrease in the ferroelectric polarization as computed by the Berry-phase method.²⁷

According to the computed Kohn–Sham (K–S) energy, the antiferromagnetic (AF) state corresponds to the spin ground-state and is more stable than the paramagnetic state by 115.96 meV per Mn ion. However, the difference in the computed K–S energy between the ordered ferromagnetic (FM) and AF states is negligibly small, less than 0.002 meV per Mn ion (for 7.4 atom % Mn-doping). This result is somewhat different from the previous result done at a higher Mn-doping level of 25 atom %,¹⁸ where the AF state is the most stable phase with the enhanced K–S energy difference ($E_{FM} - E_{AF} > 0$) of ~ 3.5 meV per Mn ion. By extrapolating these two results to our experimental Mn-doping level (2 atom %), one can conjecture that the FM spin configuration is even more stable than the AF state at 2 at.% Mn-doping, which is consistent with our experimental result of a weak FM hysteresis curve (Figure 2b).

Concerning with ferroic responses, we first examined ferroelectric and magnetic domains of the laterally (horizontally) aligned M-BTO nanorod. It is expected to be in a compressively strained state which is caused by the lattice misfit of 3% between the nanorod and the Nb-STO bottom-electrode substrate. Consequently, the direction of the ferroelectric polarization (\mathbf{P}) of the laterally aligned nanorod is predicted to be perpendicular to the substrate surface (Figure 4a). On the contrary, the direction of the magnetization (\mathbf{M})

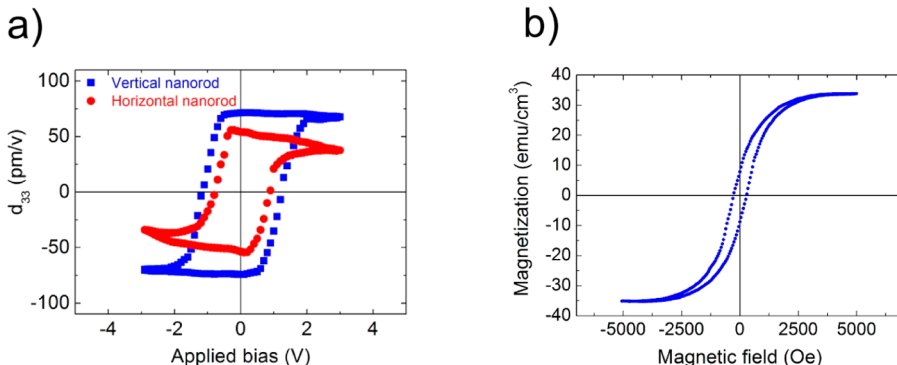


Figure 2. (a) Piezoelectric hysteresis loop of the vertically aligned M-BTO nanorod at 300 K is compared with that of the laterally aligned nanorod. (b) Magnetization-field (M-H) hysteresis loop of the vertically aligned M-BTO nanorods array at 300 K.

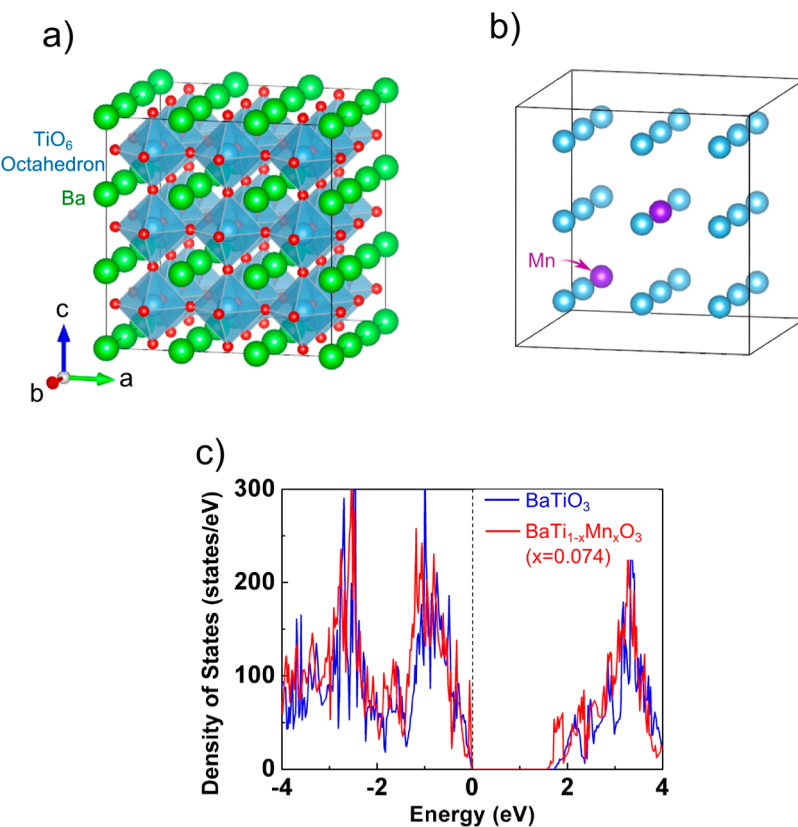
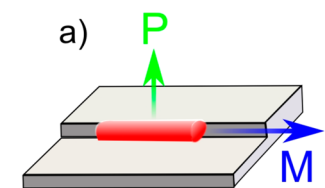


Figure 3. (a) Optimized $3a \times 3b \times 3c$ supercell structure of the ferroelectric $P4mm$ BaTiO_3 (BTO). The lattice parameters adopted in our DFT calculations are $a = b = 3.997 \text{ \AA}$ and $c = 4.0413 \text{ \AA}$.²⁸ (b) The substitution pattern of Mn-doped BTO ($\text{BaTi}_{1-x}\text{Mn}_x\text{O}_3$) for $x = 0.074$, *i.e.*, 7.4 atom % Mn-doping. In the present DFT calculations, we adopted a $3a \times 3b \times 3c$ supercell with the thin-film boundary condition along the c -axis (*i.e.*, vacuum for z greater than $3c$). The ferroelectric polarization as computed by applying the Berry-phase method²⁷ is $22 \mu\text{C}/\text{cm}^2$ for the pure BTO while it reduces to half of its original value ($\sim 11 \mu\text{C}/\text{cm}^2$) at 7.4 atom % Mn-doping. This qualitatively explains the experimental observation made for undoped and Mn-doped BTO thin films.²⁰ (c) The computed total density of states of BaTiO_3 and $\text{BaTi}_{1-x}\text{Mn}_x\text{O}_3$ ($x = 0.074$). As shown in the figure, the band gap (E_g) decreases slightly upon the addition of Mn to the pure BaTiO_3 : 1.72 eV for undoped BTO and 1.57 eV for 7.4 atom % Mn-doped BTO. This indicates that the M-BTO is insulating at 2 atom % Mn-doping (experimental doping level). This supports the piezoelectric hysteresis loop presented in Figure 2a.

is parallel to the substrate surface as the magnetic easy axis should be parallel to the axis direction of the laterally aligned nanorod having a high aspect ratio. Figure 4b presents an atomic force microscopy (AFM) image of five selected M-BTO nanodots formed laterally on a Nb-STO substrate. It is estimated that the diameter and the length of the M-BTO nanodot are about 27 and 80 nm, respectively. A magnetic force microscopy (MFM) image obtained with the MFM tip polarized upward (Figure 4c) indicates that the laterally aligned M-BTO nanodot is characterized by a single magnetic domain with the magnetization parallel to the axis direction of the nanodot. Piezoelectric force microscopy (PFM) study further indicates that the laterally aligned nanodot is characterized by 180° ferroelectric domains with the polarization direction vertical to the axis direction of the nanodot (Figure 4d,e). Thus, the direction of \mathbf{P} of the laterally aligned nanodot is perpendicular to the direction of \mathbf{M} , thus, to the substrate surface. This conclusion is consistent with the previous prediction summarized in Figure 4a.

We then examined ferroelectric and magnetic responses of the vertically aligned M-BTO nanorods array. In this case, the direction of \mathbf{M} is perpendicular to the substrate surface as the magnetic easy axis should be parallel to the axis direction of the vertical nanorod having a high aspect ratio. The [001] polar direction of the vertically aligned M-BTO nanorod having 4-fold tetragonal symmetry is also parallel to the axis direction [Figure 1e,f and Figure 2a]. Thus, the direction of \mathbf{P} is predicted to be either parallel or antiparallel to \mathbf{M} , as schematically depicted in Figure 5a. Figure 5b presents an AFM image of the AAO nanotemplate used in the fabrication of the vertically aligned M-BTO nanorods array, showing its pore diameter of about 30 nm. These nanopores are filled with the M-BTO nanorods (Figure 5c) by utilizing the DPN method combined with subsequent drying and annealing processes. A PFM image (Figure 5d) demonstrates that the polarization (\mathbf{P}) is either parallel or antiparallel to the axis direction and, thus, is vertical to the substrate plane. A MFM image (Figure 5e) indicates that the magnetization is oriented along the axis of the



Horizontal nanorod

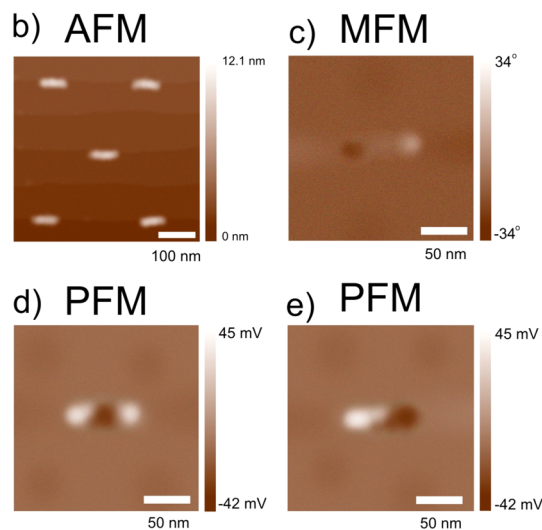
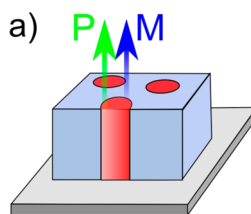


Figure 4. Laterally aligned 2 atom % Mn-doped BaTiO₃ (M-BTO) nanorods. (a) Schematic representation of the laterally aligned nanorod along a terrace edge of the Nb-doped STO substrate, indicating that the direction of **P** is perpendicular to the direction of **M**. (b) An AFM image of the M-BTO nanodots array formed laterally on the Nb-STO substrate. (c) A MFM image of the laterally aligned nanorod characterized by a single magnetic domain with **M** parallel to the nanorod axis. (d and e) PFM images of the laterally aligned M-BTO nanorod indicating the presence of 180° ferroelectric domains with the **P** direction vertical to the nanorod axis.

vertically aligned nanorod having a single magnetic domain. Accordingly, **P** is either parallel or anti-parallel to **M**, confirming the above made prediction (Figure 5a). We have further estimated the potential memory-storage capacity of the vertically aligned M-BTO nanorods array by taking into account the interpore distance (100 nm) and the nanorod diameter (30 nm) of the AAO template (Figure 5b), and it is as high as 75 Gbit/in.². Thus, the present vertical nanorods array can be used to implement high-density memory devices.

By combining two distinct polarization states with two magnetization states, one can practically implement a high-density four-states multiferroic memory using the vertically aligned M-BTO nanorods array. Figure 6a to 6d schematically depicts the four distinct ferroic states, (+P,+M), (-P,+M), (+P,-M), and (-P,-M), respectively. Because of a negligible degree of the **P**-**M** cross-coupling in the M-BTO nanorod, the direction and magnitude of the magnetization is not influenced by the electric-field-induced **P** switching, namely, (+P,+M)_{-E} ↔ +E(-P,+M) and (+P,-M)_{-E} ↔



Vertical nanorod

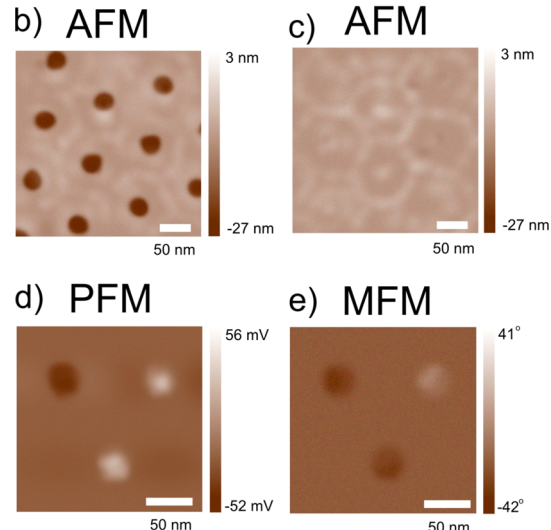


Figure 5. Vertically aligned 2 atom % Mn-doped BaTiO₃ (M-BTO) nanorods. (a) Schematic representation of the vertically aligned nanorods array, indicating that the direction of **P** is either parallel or antiparallel to the direction of **M**. (b) An AFM image of the AAO nanotemplate with empty holes for the M-BTO nanorods array. (c) An AFM image of the AAO nanotemplate filled with the vertically aligned M-BTO nanorods. (d) A PFM image of the vertically aligned M-BTO nanorods with their **P** vectors vertical to the substrate plane. (e) A MFM image of the vertically aligned M-BTO nanorods with their **M** vectors either parallel or antiparallel to the **P** direction.

+E(-P,-M), as schematically depicted in Figure 6a ↔ 6b and Figure 6c ↔ 6d, respectively. Similarly, the direction and magnitude of the ferroelectric polarization is predicted to be unaffected by the magnetic-field-induced **M** switching, namely, (+P,+M)_{-H} ↔ +H(+P,-M) and (-P,+M)_{-H} ↔ +H(-P,-M), as schematically depicted in Figure 6a ↔ 6c and Figure 6b ↔ 6d, respectively.

The four distinct multiferroic states in the vertically aligned M-BTO nanorod are demonstrated using PFM and MFM techniques (Figure 6e–h). For instance, Figure 6g shows an upward **P** and a downward **M** which corresponds to a (+P,-M) state, as schematically depicted in Figure 6c. Accordingly, the PFM and MFM images presented in Figure 6, panels e, f, g, and h, respectively, represent (+P,+M), (-P,+M), (+P,-M), and (-P,-M) states which, in turn, correspond to Figure 6, panels a, b, c, and d, respectively. Here, it is important to emphasize that the **M** switching in the M-BTO nanorod can be detected by MFM without having a great deal of difficulty since the present nanorod is characterized by a single magnetic domain.

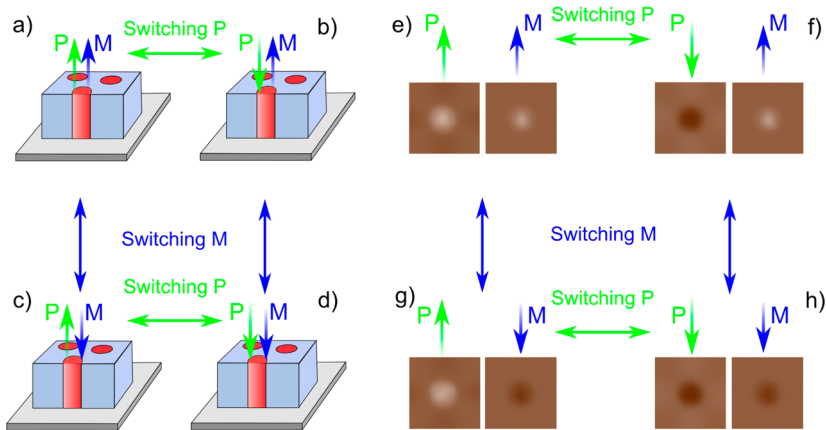


Figure 6. Implementation of a high-density four-states multiferroic memory using the vertically aligned M-BTO nanorods array. (a–d) Schematic drawing of four distinct ferroic memory states implemented using the vertically aligned nanorods array. (e–h) PFM and MFM images of the vertically aligned M-BTO nanorod with distinct ferroic states. The PFM and MFM images presented in panels e, f, g, and h, correspond to panels a, b, c, and d, respectively.

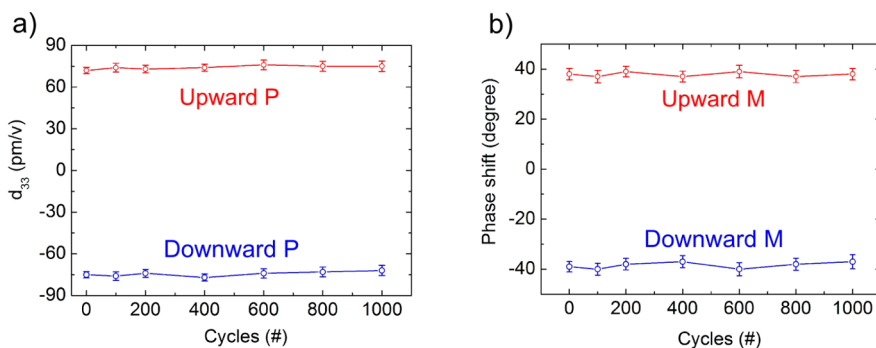


Figure 7. (a) The piezoelectric constant, d_{33} , of the vertically aligned M-BTO nanorod plotted as a function of the polarization-switching cycle. (b) The measured phase shift at the MFM tip plotted as a function of the magnetic-switching cycle.

In the case of a multiferroic thin film having weak ferromagnetism characteristics such as BiFeO_3 ,^{29,30} however, it is very difficult to detect the **M** switching because of a faint MFM signal from the ferromagnetic multodomains having a mosaic structure, in general.

To assess the device reliability of the present M-BTO nanorods array toward multistates nonvolatile memory applications, we have examined memory-retention characteristics against the switching. As shown in Figure 7a, for both upward and downward polarizations, the piezoelectric constant, d_{33} , is well retained up to 10^3 switching cycles, demonstrating a desirable electrical fatigue resistance of the vertically aligned M-BTO nanorod. On the other hand, the reliability in the magnetic memory can be conveniently assessed by examining the phase shift of the oscillating MFM tip (at 35 kHz) as a function of the magnetic-switching cycle. As shown in Figure 7b, for both upward and downward magnetizations, the phase shift remains

essentially unchanged up to 10^3 switching cycles, showing a reliable magnetic fatigue resistance of the present M-BTO nanorods array against the **M** switching.

CONCLUSIONS

A high-density four-states multiferroic memory has been demonstrated using 2 atom % Mn-doped BTO nanorods array fabricated by applying the DPN method. The vertically aligned nanorod is characterized by tetragonal symmetry with (i) the unique *c*-axis along the axis direction of the nanorod and with (ii) the **P** direction either parallel or antiparallel to the **M** direction. By suitably exploiting this directional property and a negligible degree of the **P**–**M** cross-coupling, we have successfully implemented four distinct multiferroic memory states, $(+P,+M)$, $(+P,-M)$, $(-P,+M)$, and $(-P,-M)$, using the vertically aligned nanorod. The reliability in the **P** and **M** switching was demonstrated by examining the switching-cycle-dependent piezoelectric and magnetic responses.

METHODS

Fabrication of Nanorods. For the fabrication of the laterally aligned M-BTO nanorods, we suitably combined the DPN

method with a ‘step-edge decoration’ technique.^{23,24} This step-edge decoration technique is efficient to form nanorods along the terrace edge. On the other hand, the vertically aligned

M-BTO nanorods array was fabricated using an AAO nanotemplate. To make an atomically flat surface of the Nb-doped SrTiO_3 (STO) substrate (Nb-doping level of ~ 1 wt % with the resistivity of $\sim 0.001 \Omega \cdot \text{cm}$) which is also used as a bottom electrode for the M-BTO nanorods, the Nb-doped STO substrate was rinsed in a dilute HF solution and subsequently annealed at 1000°C for 1 h. A 100-nm-thick AAO nanotemplate with the pore diameter of ~ 30 nm and the interpore distance of ~ 100 nm was subsequently prepared on a Nb-doped STO substrate by the four-step anodization of a $1.6\text{-}\mu\text{m}$ -thick Al film with an anodization voltage of 40 V at 15°C (see Figure S1 of Supporting Information). For the DPN process of M-BTO nanorods, we used a sharp Si_3N_4 DPN tip which is slightly less than 10 nm in its radius. After forming precursor-sol nanorods on a Nb-doped STO substrate, we slowly dried these precursor-sol nanorods for a day at room temperature. For the subsequent crystallization, we quickly annealed these M-BTO nanorods in oxygen atmosphere at 700°C for 1 h.

AFM Characterizations. Morphological features of the M-BTO nanorods were examined using an atomic force microscope equipped with a sharp Si_3N_4 tip (tip radius less than 5 nm). Piezoelectric force microscopy (PFM) measurements were carried out to investigate the ferroelectric switching responses of the M-BTO nanorods by switching and subsequent reading of the ferroelectric domain under an applied electric field. A platinum-coated Si_3N_4 conducting tip (tip radius ~ 20 nm, tip height $15\text{ }\mu\text{m}$, resonance frequency ~ 80 kHz, and spring constant $\sim 0.65\text{ N/m}$; MIKROMASCH) with a constant scanning speed of 50 nm/s was used in PFM measurements. To investigate ferromagnetic properties in nanometer scale, we performed magnetic force microscopy (MFM) measurements for both vertically and laterally aligned M-BTO nanorods. For this purpose, Co-coated Si_3N_4 cantilevers (with a force constant k of $\sim 2.1\text{ N/m}$ and a resonance frequency of 35 kHz) were used. During the MFM measurements, the distance between the MFM tip and the surface was uniformly maintained at a fixed distance of 50 nm using the surface topography obtained by noncontact AFM measurements. The MFM tip was sinusoidally oscillated at a frequency of 35 kHz but with its amplitude smaller than the amplitude used in the noncontact AFM measurements. The MFM signals were obtained by reading the phase shift of the oscillating MFM tip which is induced by the magnetic interaction between the MFM magnetization and the magnetic domains in a sample.

First-Principles Calculations. We have carried out first-principles DFT calculations on the basis of the generalized gradient approximation (GGA) method²⁵ implemented in the projector augmented wave (PAW) pseudopotential²⁶ using the Vienna *ab initio* simulation package (VASP).³¹ All the DFT calculations were performed using (i) a $5 \times 5 \times 5$ Monkhorst-Pack k -point mesh centered at Γ , (ii) a 500 eV plane-wave cutoff energy, and (iii) the tetrahedron method with the Blöchl corrections for the Brillouin zone integrations.³² We explicitly treated 10 valence electrons for Ba ($5s^25p^66s^2$), 4 for Ti ($3d^44s^2$), 7 for Mn ($3d^54s^2$), and 6 for O ($2s^22p^4$). The structural optimizations were performed for the 135 atoms by adopting a $3a \times 3b \times 3c$ BaTiO_3 supercell. The ions were relaxed without any symmetry constraint until the forces on them were less than $0.01\text{ eV}/\text{\AA}$.

Conflict of Interest: The authors declare no competing financial interest.

Acknowledgment. This work was supported by the Brain Korea 21 Project and by the Korea Research Foundation Grant under contract no. KRF-2008-313-C00309. This research was also supported by the WCU (World Class University) program by the Korea Research Foundation (Grant No. R31-2008-000-10059-0) of Korea. Computational resources provided by KISTI Supercomputing Centre (Project No. KSC-2012-C2-22) of Korea are gratefully acknowledged.

Supporting Information Available: Detailed description of anodizing AAO nanotemplate for the vertically aligned nanorods array. This material is available free of charge *via* the Internet at <http://pubs.acs.org>.

REFERENCES AND NOTES

- Wang, J.; Neaton, J. B.; Zheng, H.; Nagarajan, V.; Ogale, S. B.; Liu, B.; Viehland, D.; Vaithyanathan, V.; Schlom, D. G.; Waghmare, U. V.; *et al.* Epitaxial BiFeO_3 Multiferroic Thin Film Heterostructures. *Science* **2003**, *299*, 1719–1722.
- Kimura, T.; Goto, T.; Shintani, H.; Ishizaka, K.; Arima, T.; Tokura, Y. Magnetic Control of Ferroelectric Polarization. *Nature* **2003**, *426*, 55–58.
- Hur, N.; Park, S.; Sharma, P. A.; Ahn, J. S.; Guha, S.; Cheong, S.-W. Electric Polarization Reversal and Memory in a Multiferroic Material induced by Magnetic Fields. *Nature* **2004**, *429*, 392–395.
- Lottermoser, T.; Lonkai, T.; Amann, U.; Hohlwein, D.; Ihringer, J.; Fiebig, M. Magnetic Phase Control by an Electric Field. *Nature* **2004**, *430*, 541–544.
- Zheng, H.; Wang, J.; Lofland, S. E.; Ma, Z.; Mohaddes-Ardabili, L.; Zhao, T.; Salamanca-Riba, L.; Shinde, S. R.; Ogale, S. B.; Bai, F.; *et al.* Multiferroic $\text{BaTiO}_3\text{-CoFe}_2\text{O}_4$ Nanostructures. *Science* **2004**, *303*, 661–663.
- Tokura, Y. Multiferroics as Quantum Electromagnets. *Science* **2006**, *312*, 1481–1482.
- Eerenstein, W.; Mathur, N. D.; Scott, J. F. Multiferroic and Magnetoelectric Materials. *Nature* **2006**, *442*, 759–765.
- Cheong, S.-W.; Mostovoy, M. Multiferroics: a Magnetic Twist for Ferroelectricity. *Nat. Mater.* **2007**, *6*, 13–20.
- Ishiwata, S.; Taguchi, Y.; Murakawa, H.; Onose, Y.; Tokura, Y. Low-Magnetic-Field Control of Electric Polarization Vector in a Helimagnet. *Science* **2008**, *319*, 1643–1646.
- Tokunaga, Y.; Furukawa, N.; Sakai, H.; Taguchi, Y.; Arima, T.; Tokura, Y. Composite Domain Walls in a Multiferroic Perovskite Ferrite. *Nat. Mater.* **2009**, *8*, 558–562.
- Fennie, C. J. Ferroelectrically induced Weak Ferromagnetism by Design. *Phys. Rev. Lett.* **2008**, *100*, 167203.
- Lebeugle, D.; Colson, D.; Forget, A.; Viret, M.; Bataille, A. M.; Gukasov, A. Electric-field-induced Spin Flop in BiFeO_3 Single Crystals at Room Temperature. *Phys. Rev. Lett.* **2008**, *100*, 227602.
- Yun, K. Y.; Ricinschi, D.; Kanashima, T.; Okuyama, M. Enhancement of Electrical Properties in Polycrystalline BiFeO_3 Thin Films. *Appl. Phys. Lett.* **2006**, *89*, 192902.
- Catalan, G.; Scott, J. F. Physics and Applications of Bismuth Ferrite. *Adv. Mater.* **2009**, *21*, 2463–2485.
- Lee, S.; Ratcliff, W.; Cheong, S.-W.; Kiryukhin, V. Electric Field Control of the Magnetic State in BiFeO_3 Single Crystals. *Appl. Phys. Lett.* **2008**, *92*, 192906.
- Béa, H.; Bibes, M.; Barthélémy, A.; Bouzehouane, K.; Jacquet, E.; Khodan, A.; Contour, J.-P.; Fusil, S.; Wyczisk, F. Influence of Parasitic Phases on the Properties of BiFeO_3 Epitaxial Thin Films. *Appl. Phys. Lett.* **2005**, *87*, 072508.
- Evans, D. M.; Schilling, A.; Kumar, A.; Sanchez, D.; Ortega, N.; Arredondo, M.; Katiyar, R. S.; Gregg, J. M.; Scott, J. F. Magnetic Switching of Ferroelectric Domains at Room Temperature in Multiferroic PZTFT. *Nat. Commun.* **2013**, *4*, 1534.
- Nakayama, H.; Katayama-Yoshida, H. Theoretical Prediction of Magnetic Properties of $\text{BaTi}_{1-x}\text{M}_x\text{O}_3$ ($\text{M} = \text{Sc}, \text{V}, \text{Cr}, \text{Mn}, \text{Fe}, \text{Co}, \text{Ni}, \text{Cu}$). *Jpn. J. Appl. Phys.* **2001**, *40*, L1355–L1358.
- Tong, X.; Lin, Y.-H.; Zhang, S.; Wang, Y.; Nan, C.-W. Preparation of Mn-doped BaTiO_3 Nanoparticles and Their Magnetic Properties. *J. Appl. Phys.* **2008**, *104*, 066108.
- Lin, Y.-H.; Yuan, J.; Zhang, S.; Liu, J.; Wang, Y.; Nan, C.-W. Multiferroic Behavior Observed in Highly Orientated Mn-doped BaTiO_3 Thin Films. *Appl. Phys. Lett.* **2009**, *95*, 033105.
- Piner, R. D.; Zhu, J.; Xu, F.; Hong, S.; Mirkin, C. A. Dip-Pen Nanolithography. *Science* **1999**, *283*, 661–663.
- Son, J. Y.; Shin, Y.-H.; Ryu, S.; Kim, H.; Jang, H. M. Dip-Pen Lithography of Ferroelectric PbTiO_3 Nanodots. *J. Am. Chem. Soc.* **2009**, *131*, 14676–14678.
- Petrovykh, D. Y.; Himsel, F. J.; Jung, T. Width Distribution of Nanowires Grown by Step Decoration. *Surf. Sci.* **1998**, *407*, 189–199.
- Blanc, M.; Kuhnke, K.; Marsico, V.; Kern, K. Probing Step Decoration by Grazing-incidence Helium Scattering. *Surf. Sci.* **1998**, *414*, L964–L969.

25. Perdew, J. P.; Burke, K.; Wang, Y. Generalized Gradient Approximation for the Exchange-Correlation Hole of a Many-Electron System. *Phys. Rev. B* **1996**, *54*, 16533–16539.
26. Kresse, G.; Joubert, D. From Ultrasoft Pseudopotentials to the Projector Augmented-Wave Method. *Phys. Rev. B* **1999**, *59*, 1758–1775.
27. King-Smith, R. D.; Vanderbilt, D. Theory of Polarization of Crystalline Solids. *Phys. Rev. B* **1993**, *47*, 1651–1654.
28. Kwei, G. H.; Lawson, A. C.; Billinge, S. J. L.; Cheong, S. W. Structures of the Ferroelectric Phases of Barium Titanate. *J. Phys. Chem.* **1993**, *97*, 2368–2377.
29. Kibień, I.; Kowalczyk, R.; Przeslawski, J. AFM Observations of Domain Structures in Thin Films of BiFeO₃. *Ferroelectrics* **2011**, *418*, 76–81.
30. Sung, K. D.; Park, Y. A.; Seo, M. S.; Jo, Y.; Hur, N.; Jung, J. H. Observation of Intriguing Exchange Bias in BiFeO₃ Thin Films. *J. Appl. Phys.* **2012**, *112*, 033915.
31. Kresse, G.; Furthmüller, J. Effective Iterative Schemes for *ab Initio* Total-Energy Calculations Using a Plane-Wave Basis Set. *Phys. Rev. B* **1996**, *54*, 11169–11186.
32. Blöchl, P. E.; Jepsen, O.; Andersen, O. K. Improved Tetrahedron Method for Brillouin-Zone Integrations. *Phys. Rev. B* **1994**, *49*, 16223–16233.